Theoretical characterization of the kinetics of the multiphase ozonolysis of an aqueous maleic acid droplet

Rawan Abouhaidar, Denis Duflot, Céline Toubin

Aerosol Science and Technology

ISSN: (Print) (Online) Journal homepage: www.tandfonline.com/journals/uast20

Theoretical characterization of the kinetics of the multiphase ozonolysis of an aqueous maleic acid droplet

Rawan AbouHaidar, Denis Duflot & Céline Toubin

To cite this article: Rawan AbouHaidar, Denis Duflot & Céline Toubin (2024) Theoretical characterization of the kinetics of the multiphase ozonolysis of an aqueous maleic acid droplet, Aerosol Science and Technology, 58:4, 337-355, DOI: 10.1080/02786826.2023.2286341

To link to this article: https://doi.org/10.1080/02786826.2023.2286341

AEROSOL SCIENCE AND TECHNOLOGY
2024, VOL. 58, NO. 4, 337–355
https://doi.org/10.1080/02786826.2023.2286341

Theoretical characterization of the kinetics of the multiphase ozonolysis of an aqueous maleic acid droplet

Rawan AbouHaidar, Denis Duflot, and Céline Toubin

CNRS, UMR 8523 – PhLAM – Physique des Lasers Atomes et Molécules, Univ. Lille, Lille, France

ABSTRACT

Understanding the heterogeneous reactions and transformations between organic particles and gas–phase oxidants, such as ozone, within atmospheric aqueous phases is of crucial importance. However, investigating the aerosol/droplet phase presents significant challenges in distinguishing between interfacial and bulk scenarios in laboratory studies. In the present study, the physiochemical properties and heterogeneous ozone oxidation of multiphase reactions in a water droplet containing maleic acid (MA) are investigated by means of both classical and quantum methods. The relative occurrence of interfacial and bulk reactions is dependent on the bulk affinity of O_3 and the interfacial affinity of reacting MA, which is predominantly found in the bulk phase. Reaction energetics and rate coefficients have been evaluated in different environments (gas phase, at the particle interface, and in the bulk) using a multilevel approach. The presence of interfacial water molecules enhances the initial reaction step of MA + O_3, with a larger rate coefficient at the air–water interface than in the gas phase. By assuming a Langmuir–Hinshelwood behavior and comparing it with the bulk, the ozonolysis of maleic acid mainly occurs in the bulk with rate coefficients of the order of 10^{-19} and 10^{-16} $cm^3.molecule^{-1}.$ s^{-1}, respectively. The calculated rate coefficients are compared with reported values. The original method presented here quantifies the influence of a specific heterogeneous environment on the reaction rates taking into account explicit solvation.

GRAPHICAL ABSTRACT

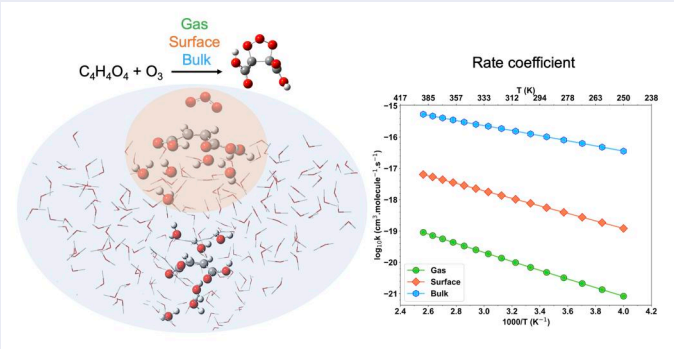

ARTICLE HISTORY
Received 25 July 2023
Accepted 7 November 2013

EDITOR
Cari Dutcher

1. Introduction

Atmospheric aerosols are important components of the climate system (IPCC 2023). They impact the radiative balance of the Earth, directly by light scattering and absorption, and indirectly by cloud formation and constitute a major human health concern (Pöschl 2005; Rosenfeld et al. 2014; Shiraiwa et al. 2017). Depending on the environment, organic compounds represent about 20–90% of the submicron aerosol mass (Kanakidou et al. 2005; Riipinen et al. 2012). Volatile Organic Compounds (VOCs) emitted into the atmosphere from anthropogenic and biogenic sources play a major role in atmospheric photochemical reactions, contributing to ozone formation (Zhang et al. 2019).

CONTACT Céline Toubin celine.toubin@univ-lille.fr Univ. Lille, CNRS, UMR 8523 – PhLAM – Physique des Lasers Atomes et Molécules, F–59000 Lille, France.

Supplemental data for this article can be accessed online at https://doi.org/10.1080/02786826.2023.2286341.

For climate models to accurately represent the behavior of aerosols in a dynamic atmosphere, it is crucial to incorporate not only the diverse composition of organic components but also the time-dependent changes in their parameters and properties, which occur through chemical reactions. Of particular significance is the role of heterogeneous chemistry involving essential atmospheric oxidants such as O_3, NO_3, and OH (Kroll and Seinfeld 2008). These reactions play a central role in the regulation of gas concentrations in the atmosphere and significantly influence aerosol particles by altering their volatilities and hygroscopic properties through the formation of reaction products (Chapleski et al. 2016).

Indeed, ozonolysis of unsaturated organic compounds is considered as a significant source of secondary organic aerosols (SOAs). Generally, it is perceived to take place *via* the "Criegee mechanism" (Criegee 1975; Pfeifle et al. 2018), which involves a series of intermediate reactions leading to the formation of various products. In the gas phase, the secondary species formed during ozonolysis may initially be volatile, but also may undergo further reactions or partition into the condensed phase (Srivastava et al. 2022). Moreover, different model simulations and laboratory studies have emphasized the role of heterogeneous reactions and the significance of water molecules in the ozonolysis process (Chen et al. 2008; Huang et al. 2023; X. Wang et al. 2020).

Low molecular weight dicarboxylic acids are important organic compounds present in atmospheric aerosol particles (Sempere and Kawamura 1996). These acids constitute a substantial portion of water-soluble organic carbon (WSOC) and predominantly remain in the particle phase due to their low vapor pressures and high solubility (Alang et al. 2023). Their presence within the particle phase enables them to participate in various chemical processes within the aqueous aerosol phase. Among aliphatic unsaturated diacids, maleic acid (MA) serves as a valuable tracer for four-carbon dicarboxylic acids in atmospheric aerosols (Sato et al. 2021; G. Wang and Kawamura 2005). It has been detected in both urban and rural aerosols, with concentrations typically measured in a few ng/m^3 (Nájera, Percival, and Horn 2009 and references therein). Interestingly, these concentrations tend to be higher under urban summer conditions, suggesting an enhanced significant production of MA in summertime compared to winter. Indeed, maleic acid is primarily produced through the photo-oxidation of benzene, toluene, and naphthalene, predominantly originating from car exhaust emissions (Dennis-Smither et al. 2014; Sato et al. 2021). Additionally, it has been suggested that maleic acid can also be produced through the hydrolysis of maleic anhydride within aerosol-containing water (Pavarelli et al. 2015; Wojcieszak et al. 2015).

The heterogeneous oxidation of maleic acid by ozone has been extensively studied experimentally. Pope et al. (2010) found that only aqueous MA aerosols experienced a loss of aerosol mass due to the production of volatile ozonolysis products, while solid aerosols showed no such effect. Previous studies have also explored the chemical and kinetic mechanisms of the ozonolysis of maleic acid in the condensed phase (Dennis-Smither et al. 2014; Gallimore et al. 2011; Nájera, Percival, and Horn 2009, 2010). Building on this, Chan and Chan (2012) investigated the influence of particle-phase state and water content on the ozonolysis of mixed maleic acid/ammonium sulfate (MA/AS) particles. Their findings revealed that aqueous maleic acid effectively reacted with ozone, while crystalline particles exhibited no reaction and underscored the importance of studying the ozonolysis of MA in aqueous aerosol droplets. Recent research by Willis and Wilson (2022) highlighted the significance of coupled reaction, diffusion, and partitioning kinetics in determining the timescales of multiphase ozone reactions. They reported a bulk reaction predominance based on the depletion of bulk-phase ozone for aqueous MA.

Considering that the importance of a reaction in the atmosphere depends not only on the yield of its products, which are more soluble and inclined to remain in the aqueous phase, but also on its reaction rate, it is crucial to understand the chemical reactions and transformations between organic particles and ozone. However, understanding the process of aqueous phase ozonolysis of MA presents challenges in distinguishing between interfacial and bulk scenarios. Thus, a comprehensive investigation of the entire story of aqueous phase ozonolysis of MA is underway, potentially changing the scope of previous multiphase chemical models. This necessitates the consideration of multiphase reactions in atmospheric phases, encompassing kinetic processes between the gas-phase, the particle interface, and its bulk.

In the present study, the reaction mechanism and kinetics for the reaction of O_3 with maleic acid at the molecular scale, in both gas phase and aqueous phase, are investigated by using the multilevel quantum chemistry approach on relevant geometries extracted from classical Molecular Dynamics (MD) trajectories. The first section describes the computational details

starting with the molecular dynamics sampling and followed by the electronic structure methodology and the kinetic calculations. Results are then presented. First, classical molecular dynamics provide insight on the partitioning of maleic acid between gas, surface and bulk phases. Based on these results, the design of the model to be used in quantum chemistry is then explained. The energetics of the reaction and the subsequent kinetics for the various environments is then presented. Atmospheric implications are briefly discussed before conclusion.

2. Computational methods

2.1. Molecular dynamics simulations

Classical molecular dynamics (MD) simulations were conducted to generate dilute maleic acid solutions resembling maleic acid water droplets that may be found either in the atmosphere or generated experimentally (Dennis-Smither et al. 2014). The MD calculations have been performed on the protonated form of the weak acid, even though partitioning into the droplet phase may be influenced by acidic conditions and subsequent deprotonations (Pye et al. 2020). However, it is to specify that in the Quantum-Mechanical (QM) treatment described thereafter, dissociation of the diacid is allowed.

Molecular interaction parameters were based on the All-Atom Optimized Potentials for Liquid Simulations (OPLS/AA) force field (Jorgensen, Ulmschneider, and Tirado-Rives 2004) in combination with the SPC/E water model (Berendsen, Grigera, and Straatsma 1987). Maleic Acid (MA) partial charges are derived from the Restrained Electrostatic Potential (RESP) approach (Bayly et al. 1993; Cieplak et al. 1995) obtained *via* quantum calculations at the M06-2X/6-311++G** level with a Polarizable Continuum Model (PCM) (Tomasi, Mennucci, and Cammi 2005), performed with the Gaussian 16 software (Frisch et al. 2016). Lorentz–Berthelot combination rules (Berthelot 1889; Lorentz 1881) were used to describe the Lennard–Jones σ and ε parameters for the corresponding atom pairs between the solute and the solvent. The force field was validated by comparing energetics and geometries of the monomers and dimers to high-level quantum chemistry calculations (see Tables S1 and S2 in the online supplementary information [SI]).

Aqueous slabs were used to model the particle interface and bulk. Molecules of maleic acid and water were randomly placed in a 4 nm size cubic box. The cell contains 1500 water molecules and 20 MA molecules. Periodic boundary conditions were applied in all three dimensions and bonds were constrained using the LINCS algorithm (Hess et al. 1997). The time step was set to 2 fs. Short-range interactions were truncated at 1.2 nm. Particle Mesh Ewald (PME) summation method (Yeh and Berkowitz 1999) with a relative tolerance of 10^{-5}, fourth-order cubic interpolation, and a Fourier spacing parameter of 0.15 were used to evaluate the long-range Coulomb interactions (dos Santos, Girotto, and Levin 2016). The temperature was held coefficient at 298 K by means of a Berendsen thermostat (Berendsen et al. 1984), with a coupling coefficient of 0.1 ps.

After minimization, a simulation in the isothermal-isobaric (NPT) ensemble at 1 atm, with Berendsen pressure coupling method, was performed to equilibrate the system for 5 ns. In order to construct the slab, the equilibrated system was placed at the center of a parallelepipedal box that was elongated along the interfacial normal direction giving box dimensions of 4 nm × 4 nm × 12 nm with two interfaces exposed to the vacuum. Then, a 5 ns annealing was performed warming the system to 450 K, and then cooling down to 298 K in the NVT ensemble. This annealing procedure enables the molecules to explore more possible configurations. Finally, a NVT trajectory was executed at 298 K for 60 ns, the last 5 ns being used to collect data for the statistical analysis. All MD calculations were performed using the GROMACS "5.1.4" program (Irrgang, Hays, and Kasson 2018).

2.2. Electronic structure calculations

Quantum Mechanical (QM) calculations were performed with the Gaussian 16 program (Frisch et al. 2016). The geometries of reactants, complexes, transition states, and products were optimized using the hybrid meta-exchange-correlation (M06-2X) functional (Zhao and Truhlar 2008a, 2008b) with the 6-311++G** basis (Davidson and Feller 1986). The M06-2X functional has previously been successfully applied to a variety of atmospheric-relevant reactions (Beste and Buchanan 2010; Dash, Balaganesh, and Rajakumar 2014; Dash and Mishra 2022; Lily et al. 2020; Zhao and Truhlar 2008b). Unscaled vibrational harmonic frequencies were used to obtain the zero-point vibrational energies (ZPEs). Minimum energy paths (MEPs) were performed in the mass-weighted Cartesian coordinates with a step size of 0.05 bohr.amu$^{1/2}$, using the intrinsic reaction coordinate (IRC) (Fukui 1981) method.

To yield more reliable reaction enthalpies and barrier heights, single-point calculations for all M06-2X/6-311++G** stationary and selected IRC points were further carried out using the Pair Natural Orbitals

based Local Coupled Cluster (PNO-LCCSD(T)-F12/cc-pVTZ-F12) (Ma et al. 2017; Schwilk et al. 2017) method (shortened to CCSD(T) in the following) with the MOLPRO (version 2019.1) package (Werner et al. 2020). The CABS single correction (Adler, Knizia, and Werner 2007) was obtained at MP2 level (Knizia and Werner 2008). The cc-pVTZ-F12 basis set (Peterson, Adler, and Werner 2008) was used with the aug-cc-pVTZ basis set for the density fitting of Coulomb, exchange and MP2 terms.

In the aqueous phase, the same procedure is used where the solvation models evolves from purely implicit, PCM model (Cossi et al. 2003; Klamt, Moya, and Palomar 2015) to fully explicit representation of the solvent, and within the framework of the ONIOM (QM/QM') method (Chung et al. 2015). The effect of solvent molecules was first quantified using the implicit solvation model (PCM) (Cossi et al. 2003; Miertuš, Scrocco, and Tomasi 1981), at the IEFPCM level (Klamt, Moya, and Palomar 2015). The ONIOM method was then applied to produce reliable geometries and energies of the solvated reaction with explicit water molecules. To this end, initial configurations were extracted from MD simulations. We divided the systems into two parts: the high-level (QM) consists in the reacting maleic acid and ozone molecules surrounded by a number of water molecules determined based on radial distribution functions, and is treated at M06-2X/6-311++G** level like gas phase; the low-level part (QM') defines an additional solvation shell and is treated at PM6 level. Only the high-level part (QM) is allowed to relax during geometry optimizations. Finally, a single point CCSD(T) as previously described, is carried out using the optimized geometries of the high-level part.

2.3. Kinetic calculations

Kinetic calculations were performed using Reaction-Path Variational Transition State Theory (RP-VTST) method within the framework of Polyrate 17–C (Zheng et al. 2017). Rate coefficients for bimolecular and unimolecular reactions over a temperature range of 250 to 400 K were calculated using the transition state theory (TST) (D. G. Truhlar, Garrett, and Klippenstein 1996), the canonical variational transition-state theory (CVT) (Bao and Truhlar 2017; D. G. Truhlar and Garrett 1984; G. Truhlar and Garrett 1987; Truong 1994), the CVT being coupled with the zero-curvature (ZCT) and small-curvature (SCT) tunneling corrections (CVT/ZCT & CVT/SCT, respectively). Rigid rotor and harmonic approximations were used in all cases. It should be noticed that in the case of explicit solvation, the partition functions of the water molecules surrounding O_3 and MA were explicitly included (see, e.g., Kannath et al. 2020). In order to obtain minimum energy paths without spurious imaginary frequencies along the reaction coordinate, redundant or non-redundant internal coordinate systems were used for generalized normal-mode analysis. Depending on the temperature of the CVT/SCT reaction rate coefficient, the results were fitted using a modified Arrhenius (Zheng and Truhlar 2010) equation:

$$k(T) = A\left(\frac{T}{300}\right)^{n} \exp\left[\frac{-E}{RT}\right] \quad (1)$$

Here, $k(T)$ is the rate coefficient, T is the temperature, and R is the ideal gas constant. A, n and E are the fitting parameters.

3. Results and discussion

3.1. Understanding the properties of an aqueous maleic acid droplet

3.1.1. Evaluation of surface preference for a single MA molecule

To evaluate the preferred residence of MA molecules in an aqueous phase, we performed a 60 ns NVT simulation focusing on a single solvated MA molecule. By tracking the time-dependent motion of the MA molecule along the z coordinate, we determine whether it is predominantly present in bulk water or migrates toward the interface (Figure 1). The simulation resulted in a dynamical behavior where the MA molecule oscillates between the water bulk and the interfaces throughout the entire simulation time frame.

Data analysis further revealed that, on average, the MA molecule spent approximately 12 ns out of the total 60 ns residing at the interfaces. From the time spent at the surface compared to the total duration of the trajectory, the probability of finding the π(C=C) bond at the surface is evaluated at 20% maximum. By dividing this probability by the area of the unit cell (1.26×10^{-13} cm^2), the surface concentration of MA, denoted as [S], was calculated to be 1.59×10^{12} molecules.cm^{-2}. The diffusion coefficient of a single MA in the aqueous slab, calculated between 2 to 10 ns along the trajectory was determined to be $1.28 \pm 0.38 \times 10^{-5}$ $cm^2.s^{-1}$. This value aligns with both previous experimental measurements and the value derived from the Stokes–Einstein equation (0.83×10^{-5} and 0.86×10^{-5} $cm^2.s^{-1}$, respectively) (Einstein 1905; Stokes 1901; Wright and Leaist 1998) (Figure S2 and Table S3).

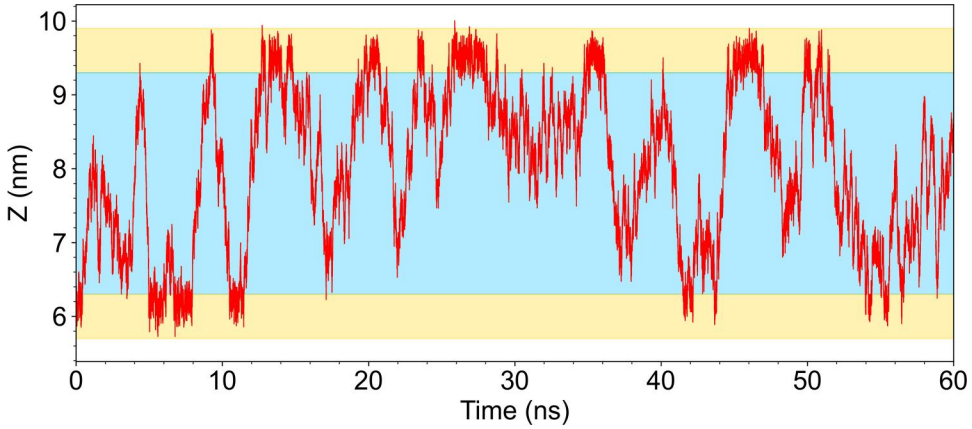

Figure 1. Time evolution of the position (z-coordinate) of one maleic acid molecule along 60 ns. The yellow area represents the interfacial region, where the water density is between 10% and 90% of its bulk value shaded in blue.

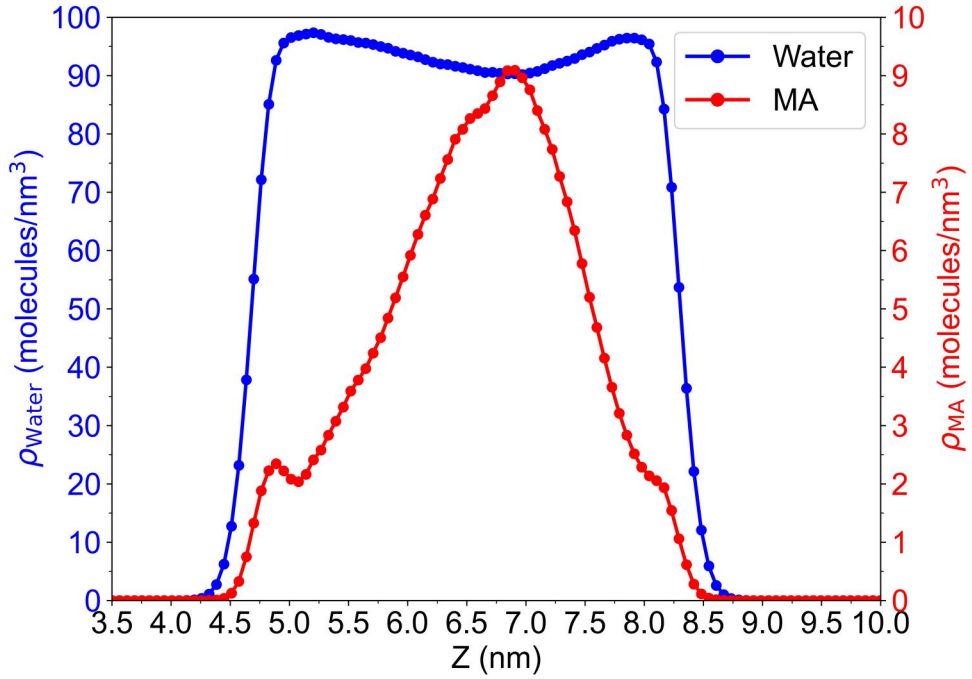

Figure 2. Density profiles from MD simulations of 20 MA in aqueous solution at 298 K.

3.1.2. Density profile

For the 20 MA aqueous solutions, the composition of the interfacial layer can be characterized by the numerical profile of a particular atom along the interfacial direction. This profile reveals whether molecules preferentially reside at the interface or in the bulk and if they exhibit a preferred orientation with respect to the interface, typically perpendicular to the z-axis. Figure 2 demonstrates the presence of maleic acid in the aqueous solution, extending from the surface layer to the bulk, where its prevalence is more pronounced.

Furthermore, defining the interfacial region as the area where the water density increases from 10% to 90% of its bulk value, we estimate the thickness (δ) of the surface layer to be 0.6 nm.

3.1.3. Energetic background and hydrogen bonds

The behavior of the acid/water system described previously can also be explained by analyzing the energy distributions for the acid – acid and acid – water interactions. These distributions are represented in Figure 3a. It should be noted that, even if this distribution is shown for only one acid molecule, the overall behavior of all acids in the system is quite similar (Figures S3 and S4).

The acid – acid binding energy (E_b) distribution ranges from 0 to -50 kcal.mol^{-1} and can be characterized by two gaussian peaks (in red in Figure 3). Specifically, a high thin peak around -10 kcal.mol^{-1} and a less pronounced one at -25 kcal.mol^{-1} can be observed. The acid–acid higher energy peak

corresponds to those located quite far from each other, that is, scattered at the surface layer of the droplet, whereas the lowest energy peak corresponds to two acids bonded through H-bonds formation. The calculated binding energy of approximately -11 kcal.mol^{-1} for two isolated maleic acids in the gas phase (Table S1) suggests that maleic acid molecules tend to form an average of one to two H-bonds with their maleic acid neighbors.

Furthermore, the energy distribution of the acid–water interactions presents two peaks as well (in blue in Figure 3). The first peak is the broadest, ranging from -20 to -60 kcal.mol^{-1}, refers to those MA molecules spreading in the subsurface layer to the interface where there is less interaction with water. The second peak is located around -80 kcal.mol^{-1} and corresponds to the strong acid–water interaction that occurs in the bulk. The observed peaks in the acid – water distribution can be attributed to the formation of multiple hydrogen bonds between acid and water molecules, since the binding energy of the isolated MA–H_2O dimer is around -7 kcal.mol^{-1} (Table S1).

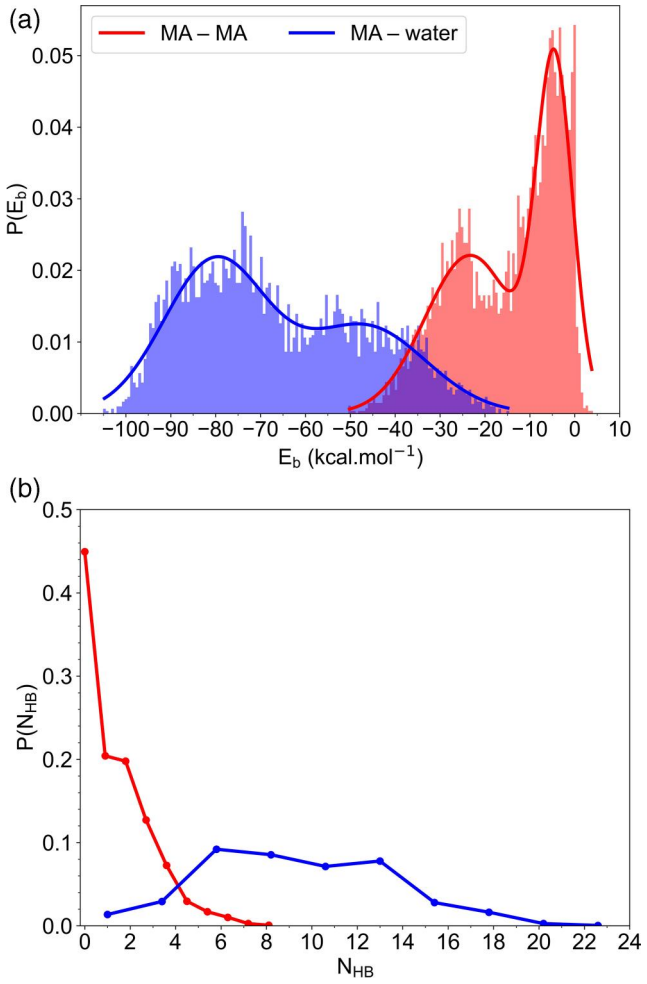

Figure 3. (a) Binding energy distributions for the MA–MA interactions and MA–H_2O interactions, and (b) probability distributions for MA to form H-bonds in aqueous solution. Red and blue curves correspond to the binding of the MA molecule with all other MA molecules and with all water molecules respectively.

This analysis shows that the energy distributions are consistent with the solubility of maleic acid in the system. The interaction between each acid with the other acids or water molecules located in their neighborhood varies, indicating that some maleic acids reach the surface while others diffuse in the bulk. Thus, we also characterized the number of hydrogen bonds that are formed either between the MA molecules or between MA and water molecules. These distributions of H-bonds are given in Figure 3b. In agreement with energy distributions, Figure 3b clearly shows that acid molecules have the flexibility to either move freely or form between one to two hydrogen bonds with their neighboring acid molecules. In addition, the number of H-bonds between acid and water molecules increases toward a higher value (between 6 to 12) in the bulk when MA is completely surrounded by water.

3.1.4. Radial distribution functions

First of all, it is important to note that MA can exist in several conformations in the gas phase, as previously shown (Maçôas et al. 2001; Nikitin, Lopes, and Fausto 2022). In the SI, we confirm that the most stable conformer of maleic acid exhibits a planar structure with C_s symmetry, which is stabilized by an intramolecular hydrogen bond (OH•••O=C) that closes a seven-membered ring (Table S4).

The MD trajectories reveal that MA molecules display different configurations and orientations as they diffuse across the entire water slab: the analysis of the snapshots and radial density functions shows four different typical conformations among the 20 dissolved maleic acids. These structures result from hydrogen bonding with water and differ from the most stable gas phase conformer. Specifically, the radial distribution function (RDF) of selected atoms displays peaks at different distances compared to gas phase due to diverse conformations and intermolecular H-bonding (Figures S5 and S6). Among these configurations, the one being closer to that in the gas phase stands out as being the most frequent configuration (55%). Therefore, we investigated the reactivity of this configuration in two different typical environments: either completely on the surface or completely dissolved in the bulk.

To prepare the aerosol phase environment for the subsequent ONIOM calculations, starting configuration that represents the maleic acid, surrounded by an explicit number of water molecules, needs to be extracted. To achieve this, coordination numbers (CN) for surface and bulk MA were extracted from RDF (Figure 4a). These CN's, shown in Figure 4b, are calculated between the MA center of mass and the water oxygen atoms over the last 100 ps of the simulation.

From Figure 4a, the surface RDF is found to be 50% smaller compared to the bulk. The first peak attributed to the nearest neighbor is similar for both situations, differences in the shape of the RDF appearing only beyond the second peak (0.27 nm). This can be attributed to the distinct environments experienced by MA molecules. In the bulk, maleic acid is indeed surrounded by a higher number of water molecules.

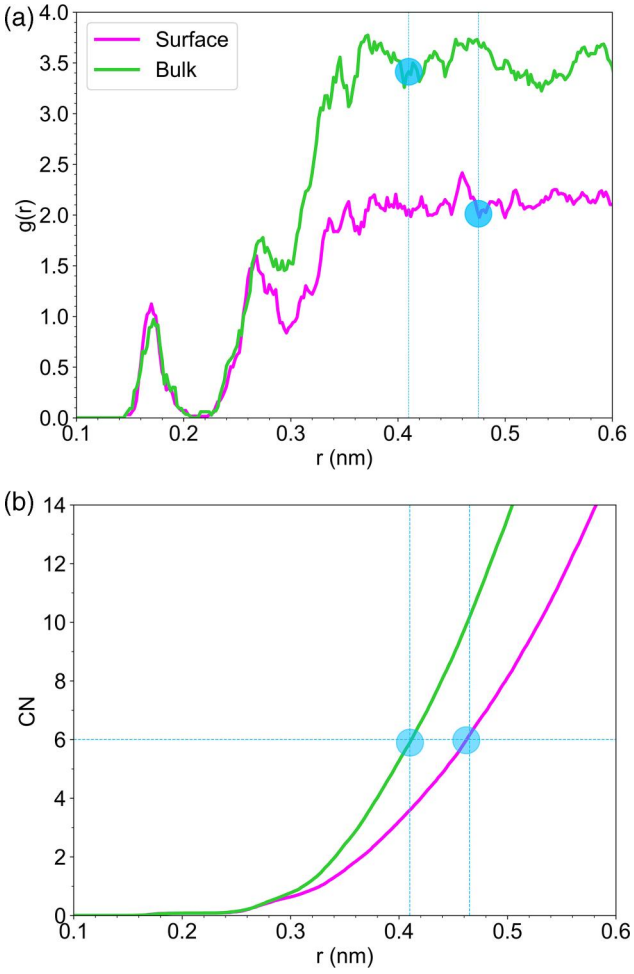

Figure 4. (a) Radial distribution functions and (b) coordination number analysis of the selected maleic acid, both on the surface and in the bulk, in relation to the water oxygens. The blue symbols correspond to the radius of the extracted formations. The RDFs were calculated for a small-time interval (100 ps) and subsequently normalized to reduce noise and improve clarity in the figure.

Based on the CN variations (Figure 4b), we selected radii of 0.41 nm and 0.47 nm for bulk and surface respectively, defining a sphere that contains 6 water molecules, for both situations, to be treated with high-level QM calculations. Additionally, we selected more water molecules within a larger distance from the MA for the low-level (QM′) calculations. This specific number of molecules is adjusted to balance both explicit solvation of the QM region and reasonable computational cost. Detailed information regarding the radii of the defined spheres and the number of molecules in each sphere can be found in the SI (Table S5).

3.2. Multiphase reaction of O_3 with aqueous maleic acid

3.2.1. Kinetics and reaction mechanism

In the case of ozonolysis, the reaction mechanism involves multiple steps, including the formation of the primary-ozonide (POZ), its subsequent decomposition, and further reactions of the Criegee intermediate (see scheme presented in Pope et al. 2010). Overall, the initial step of electrophilic addition of O_3 to the π(C=C) bond and the formation of the POZ is the first stone to set the stage for subsequent reactions and the generation of various organic compounds (Salta et al. 2022; Schank 2004; Wheeler, Ess, and Houk 2008). Before commencing our study on maleic acid, we benchmarked the 1,3-dipolar cycloadditions of ozone with ethylene in the gas phase. This preliminary study yielded appropriate rate coefficients (Tables S6–S9 and Figure S7). Therefore, we expect similar accuracy and reliability of our various present approaches used for determining the rate coefficient for MA in gas phase and further at the droplet interface or bulk.

The primary ozonolysis reaction of maleic acid follows a two-step mechanism, as described by Equation (2) where the reactive complex (RC) is assumed to be in equilibrium with the MA and O_3, and the reaction proceeds from this complex.

$$MA + O_3 \underset{\rightarrow}{\overset{K_{eq}}{\leftarrow}} RC \overset{k_{uni}}{\rightarrow} POZ \qquad (2)$$

Here, K_{eq} is the equilibrium coefficient between the reactants and the *RC* and k_{uni} is the unimolecular rate coefficient governing the formation of the *POZ*. In order to calculate K_{eq}, Gibbs free energy (ΔG) was computed at a given temperature (Equation (3)). Then, Equation (4) is used to obtain the equilibrium coefficient K_c.

$$K_{eq} = \exp\left[\frac{-\Delta G}{RT}\right] \quad (3)$$

$$K_c = K_{eq}\left(\frac{RT}{N_a}\right)^{\Delta n} \quad (4)$$

Where ΔG is the Gibbs free energy difference between reactants and RC, K_c represents the equilibrium coefficient in $cm^3.molecules^{-1}$, R is the ideal gas constant, T is the temperature, N_a is the Avogadro constant, and Δn is the change in the stoichiometric number of reactants and products (Δn = −1 in the present case).

3.2.2. Gas phase reaction

First, the reactivity of the most stable conformer of maleic acid and ozone in the gas phase was examined. Figure 5 illustrates the structural changes occurring during the reaction based on the M06-2X/6-311++G** optimized geometries. For MA, an intramolecular H-bond exists with a O–H distance of 1.66 Å. However, at the transition state (TS), a small deformation occurs, increasing the intramolecular bond length to 1.70 Å and causing a loss of planarity, finally leading to the complete breakdown of the intramolecular bond in the POZ. The potential energy surface was refined at CCSD(T) level, which revealed that the formation of the reactive complex (RC) occurs at −0.88 kcal.mol^{-1}, and the reaction is exothermic with a value of −47.39 kcal.mol^{-1}. The barrier height was determined to be 5.91 kcal.mol^{-1} (Figure 6a).

Table 1 shows the standard Gibbs free energy (ΔG°) computed at 298 K for all the reactants and RC as well as the K_{eq} and K_c coefficients. We observe that the ΔG° in gas phase is 9.34 kcal.mol^{-1} with a K_{eq} is 1.42×10^{-7}. This indicates that the reverse conversion of the RC back to ozone and MA, is thermodynamically spontaneous.

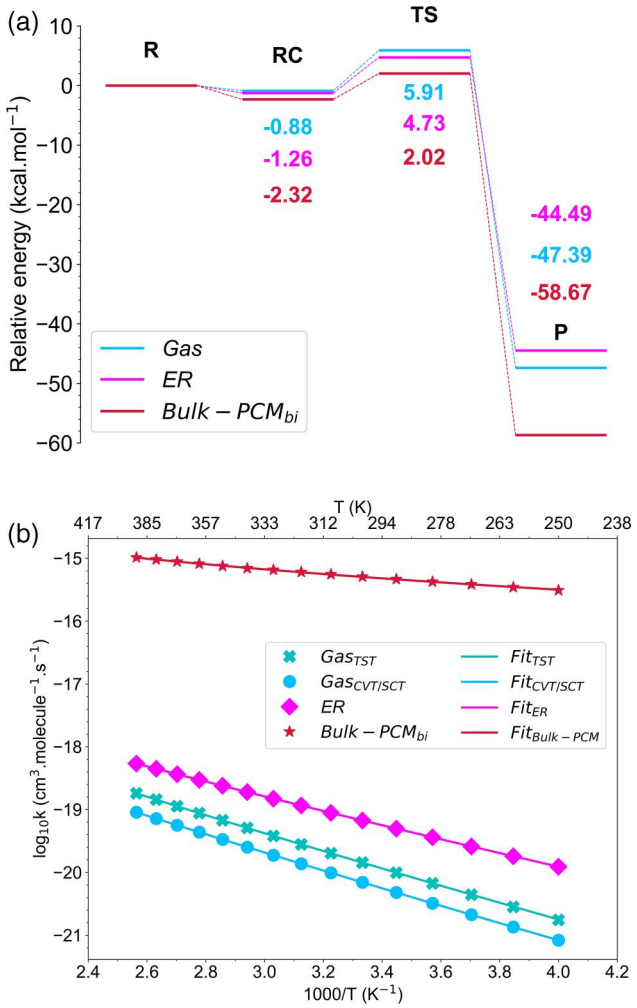

Figure 6. (a) Relative energy profile for the 1,3-dipolar cycloaddition reaction of ozone to MA in different environments: gas phase, Eley–Rideal mechanism (ER), and Bulk-PCM$_{bi}$. The potential energies, expressed in kcal.mol^{-1}, were predicted using single point CCSD(T) level and zero-point correction on DFT geometries. (b) Rate coefficients for the bimolecular reactions of O_3 + MA over a temperature range of 250–400 K. Calculations performed at the CCSD(T) level using the TST and CVT/SCT methods for the gas phase reaction, and CVT/SCT for the ER and Bulk-PCM$_{bi}$ reactions. Markers indicate the rate coefficients calculated at various temperatures, while lines correspond to the fit using the modified Arrhenius equation.

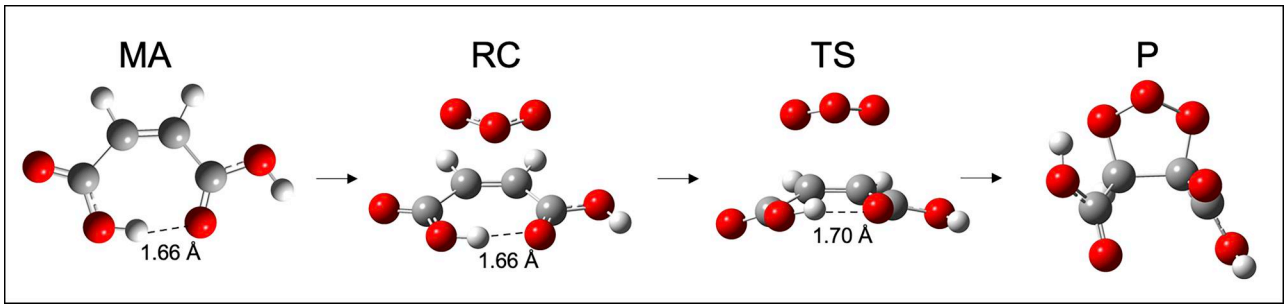

Figure 5. Structural changes of MA occurring during the gas phase O_3 + MA reaction based on the optimized geometric parameters at the M06-2X/6-311++G** level. RC, TS and P stands for reactant complex, transition state and product. Note that for the reactants at infinite distance (on the left), O_3 is not represented.

Table 1. Calculated pre-reactive complex equilibrium parameters [ΔG° (kcal.mol^{-1}), K_{eq}, and K_c (cm^3.molecules^{-1})] for the various studied environments: gas phase, surface and bulk.

	ΔG° (kcal.mol^{-1})	Keq	Kc (cm^3.molecules^{-1})
Gas phase	9.34	1.42×10^{-7}	5.78×10^{-27}
Surface	8.35	7.57×10^{-7}	3.08×10^{-26}
Bulk-PCM	6.00	3.96×10^{-5}	1.61×10^{-24}

Table 2. The fitted parameters using the modified Arrhenius equation for the primary reaction of maleic acid with ozone for the various studied environments (A in cm^3. molecule^{-1}. s^{-1} and s^{-1} for the bimolecular and the unimolecular reaction rate coefficients, respectively; E in kcal.mol^{-1}).

		Parameter		
		A	*N*	*E*
Gas phase	TST	4.26×10^{-17}	2.65	4.78
	CVT/SCT	3.29×10^{-17}	2.35	5.05
Aerosol phase	ER	3.05×10^{-17}	2.57	3.65
	Bulk-PCM$_{bi}$	2.87×10^{-16}	3.19	−0.38
	LH	2.39×10^{11}	0.03	5.47
	Bulk	9.33×10^{11}	0.02	2.79
	Bulk-PCM$_{uni}$	8.80×10^{9}	1.38	2.82

The reaction rate coefficients of O_3 with MA were investigated using various methods within the temperature range of 250–400 K and at 1 atm pressure, as illustrated in Figure 6b. The IRC points taken for rate coefficients calculations along with the results obtained from alternative methods can be found in Figure S8. We will focus on the TST and CVT/SVT results. At 298 K, the rate coefficients are 1.33×10^{-20} and 6.45×10^{-21} cm^3.molecule^{-1}. s^{-1} for TST and CVT/SCT, respectively. This indicates that the rate coefficients using CVT/SCT are approximately lower by a factor of 2 than those using TST. The tunneling factor (κ) for the 1,3-dipolar cycloaddition of ozone within the temperature range of 250 K to 400 K has been determined to be an average of 1.1. As expected, this value is comparatively lower than the tunneling factors observed in other types of reactions, such as H-abstraction, which typically range between 1.2 and 2.9 (Dash and Mishra 2022).

Furthermore, the reaction rate coefficients of MA with ozone are slower compared to other unsaturated molecules with different functional groups (Grira et al. 2022; X. Wang et al. 2021). This could be attributed to the presence of the intramolecular H-bond within MA which could cause a higher barrier and a delay in the reaction mechanism. This delay occurs because there is competition between different bonds involved in the reaction, which leads to a step where the intramolecular bond within MA breaks down. Additionally, Razumovskii and Zaikov (1980) reported that cycloalkenes with one π (C=C) bond react slightly less rapidly than compounds with a π (C=C) bond in an open chain. However, as the temperature increases, the rate coefficients also increase, exhibiting an Arrhenius behavior in the gas phase. The fitting parameters of Equation (1) are summarized in Table 2 and reaction rate coefficients at various temperature are summarized in Tables S10–S12.

3.2.3. Gas-surface reaction and Langmuir–Hinshelwood framework

For the surface processes, different mechanisms have been proposed to explain how the reaction takes place. One mechanism is the Eley–Rideal (ER) one, where ozone from the gas phase reacts directly with maleic acid present at the surface. Another mechanism is the Langmuir–Hinshelwood framework (LH), where ozone first adsorbs at the surface and then reacts with the adsorbed MA. A schematic representation of the QM/QM' description of MA at the surface of an aerosol phase and the transition state for the O_3 + MA reaction is depicted in Figure 7a.

The first scenario (ER) involves the adsorption of maleic acid at the water surface, followed by the approach of gaseous O_3 to the interface, where the two species react *via* collision. For the ER reaction, it was determined that the formation of the reactive complex (RC) takes place at an energy level of −1.26 kcal.mol^{-1}. The reaction is exothermic, releasing an energy of −44.49 kcal.mol^{-1}. The barrier height for this reaction was established as 4.73 kcal.mol^{-1}, as depicted in Figure 6a. It can be inferred that the reaction occurring at the surface is expected to proceed more rapidly, due to the fact that the surface reaction involves a lower energy barrier compared to the gas-phase reaction (4.73 < 6.82 kcal.mol^{-1}).

The rate coefficient for the ER reaction was calculated using different methods, but they yielded similar results without significant tunneling effects observed between TST and CVT/SCT. Figure 6b shows the rate coefficients obtained from the CVT/SCT method while the values obtained from different methods can be found in Tables S13–S15. Furthermore, the reaction rate coefficients were found to fit the modified Arrhenius equation (Table 2).

According to the phase diagram for water and at a standard atmospheric pressure, water exists in a liquid state within a defined temperature range of 273 to 373 K. This temperature range is particularly relevant when discussing aqueous aerosol phase reactions, as it represents the conditions where water remains in its liquid form.

Comparing the gas-phase results to the surface ones, it can be observed that the surface reaction has higher

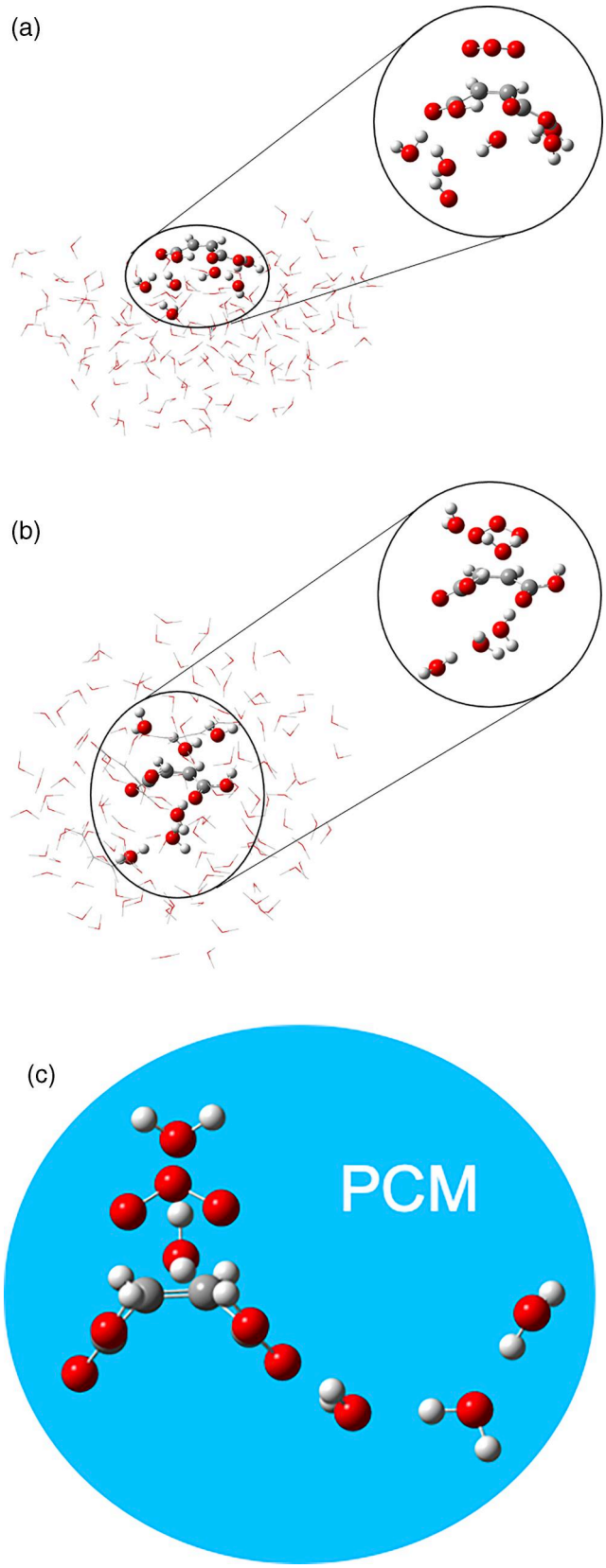

Figure 7. Molecular representation of the fully explicit QM/QM′ model at the surface (a) and the Bulk (b). (c) represents the Bulk-PCM description where the QM′ part is replaced by a dielectric continuum (PCM). The transition state in the high-level region (QM) is observed for both cases, as well as in the Bulk-PCM environment based on the optimized geometries at the M06-2X/6-311++G** level.

rate coefficients across the temperature range compared to both gas phase TST and CVT/SCT values. At 298 K, the surface rate coefficient (6.32×10^{-20} cm^3.molecule^{-1}. s^{-1}) is significantly higher compared to the gas phase one (6.45×10^{-21} cm^3.molecule^{-1}. s^{-1}), i.e., about 1 order of magnitude faster. This enhanced surface reaction rate coefficient can be attributed to the presence of water molecules, which play a crucial role in increasing the collision frequency between the reactants, thereby potentially increasing the reaction rate coefficient (Huang et al. 2023). Moreover, the computed standard Gibbs free energy (ΔG°) at 298 K for the reactants (MA at the surface and Ozone in gas phase) and the RC involved in the surface process is determined to be 8.35 kcal.mol^{-1} which is lower than the corresponding value in the gas phase. K_{eq} and K_c equilibrium coefficients are found to be 7.57×10^{-7} and 3.08×10^{-26} cm^3.molecule^{-1}, respectively (Table 1).

The second scenario (LH) considers a unimolecular reaction involving the adsorption of ozone at the air–water interface, followed by its diffusion on the surface and subsequent collision with MA. This can be modeled by using the reaction complex (RC) from the surface reaction discussed above as a reactant. The energy barrier is thus 5.99 kcal.mol^{-1} and the exoergicity between the RC and P is −43.23 kcal.mol^{-1} (Figure 8a).

At 298 K, the LH reaction rate coefficient was determined to be $2.34 \times 10^{+7}$ s^{-1}. Figure 8b presents the results obtained from the CVT/SCT method, while a summary of the values obtained from various methods can be found in Tables S16–S18. In the steady-state approximation, the corresponding forward 2nd order rate coefficient (k_{LH}) can be approximated by Equation (5):

$$k_{LH} = K_c k_{uni} \tag{5}$$

Hence, at 298 K, the LH reaction exhibits a k_{LH} of 7.21×10^{-19} cm^3.molecule^{-1}. s^{-1} which is about 1 order of magnitude larger than the ER rate coefficient. It should be noted that ER mechanism is less likely to happen compared to LH framework since it requires that ozone directly meets MA lying at the surface.

In Section 3.1, we estimated the thickness of the surface layer (δ). Therefore, the surface bimolecular rate coefficient (k_s) can be estimated using Equation (6) (Kleber, Laß, and Friedrichs 2013):

$$k_s = \frac{k}{\delta} \tag{6}$$

Where k_s is the surface bimolecular rate coefficient (cm^2.molecule^{-1}. s^{-1}), k is the 2nd order calculated rate coefficient, and δ is the estimated thickness (0.6 nm). This leads to surface reaction rate coefficients at 298 K

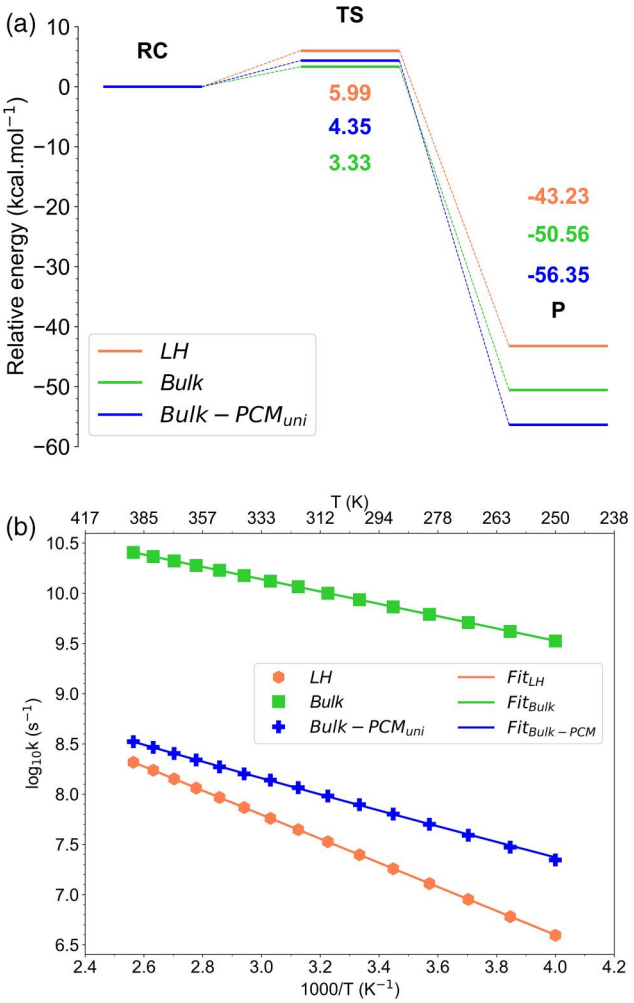

Figure 8. (a) Relative energy profiles for the 1,3-dipolar cycloaddition reaction of ozone to MA in different environments: Langmuir Hinshelwood framework (LH), ONIOM bulk and Bulk-PCM$_{uni}$. The potential energies, expressed in kcal.mol^{-1}, were predicted using the CCSD(T) level and zero-point correction on DFT geometries. (b) Rate coefficients for the unimolecular reactions of O_3 + MA over a temperature range of 250–400 K. Calculations were performed at the CCSD(T) level using the CVT/SCT method. Markers indicate the rate coefficients calculated at various temperatures, while lines correspond to the Arrhenius fit.

of 1.05×10^{-12} and 1.20×10^{-11} cm^2.molecule^{-1}. s^{-1}, for the ER and LH mechanisms, respectively.

Furthermore, the pseudo-first-order rate coefficient $k_s^{1,\max}$ can be calculated according to Equation (7) (see, e.g., Nájera, Percival, and Horn 2009, 2010):

$$k_s^{1,\max} = k_s[S] \tag{7}$$

where $k_s^{1,\max}$ is the apparent rate coefficient for the surface reaction (s^{-1}) obtained in the high-pressure limit for gaseous ozone and [S] represents the surface concentration of MA determined in Section 3.1.

Using the calculated from the Eley–Rideal rate coefficient, $k_s^{1,\max}$ is found to be 1.67 s^{-1}. This value demonstrates a reasonable agreement with the reported values by Nájera, Percival, and Horn (2009, 2010). Their studies indicate $k_s^{1,\max}$ values of $0.038 \pm 0.004\ s^{-1}$ and $0.21 \pm 0.01\ s^{-1}$ for dry and humid maleic acid aerosol particles, respectively. The conditions of the present work are closer to the humid case of Nájera et al. Moreover, the concentration of these experiments (0.65 M) is similar to the present calculations (0.61 M) so that our $k_s^{1,\max}$ is about one order of magnitude too large.

On the other hand, for the surface bimolecular Langmuir–Hinshelwood rate coefficient, $k_s^{1,\max}$ is found to be 19.08 s^{-1}, which is two orders of magnitude further away from the experimental determinations. Several reasons may explain these discrepancies. The first parameter is the value of the thickness surface layer δ. Indeed our value of 0.6 nm is 40% smaller than the commonly used value of 1 nm (Willis and Wilson 2022). Using a 1 nm thickness would decrease our $k_s^{1,\max}$ by 60% but still give too large values. The second parameter involved is the surface concentration of MA π(C=C) bonds available for the reaction, which we derive from the residence time of MA at the surface. However, the presence of one MA molecule at the surface does not necessarily guarantee that its π bond is available at the surface. For example, a recent MD study on oleic and stearic acids with water (Stewart, Paterson, and Greaves 2022) showed that only 1 to 2% of the π bonds for pure oleic are located at the surface, which reduces the surface concentration by two orders of magnitude. Although it is not possible to estimate this quantity in the present work, a decrease of the [S] value would lower our $k_s^{1,\max}$ results and bring them closer to experiments. Finally, the last parameter is the rate coefficient itself which is very sensitive to the calculated energies along the reaction path.

3.2.4. Bulk reactions

In the bulk phase, we consider a mechanism where ozone diffuses into the aqueous solution and subsequently reacts with pre-solvated MA. In this work, two different approaches were employed to investigate this process. The first one, referred to as "Bulk," utilizes a QM/QM' approach similar to the surface one. Solvation is fully explicit within this QM/QM' Bulk model. To simulate this bulk reaction, we replaced one of the surrounding water molecules by ozone, thereby assuming that ozone has diffused across the aqueous film. It is important to note that, in this context, we could only define a unimolecular reaction due to the challenge of establishing a profile where both ozone and MA are sufficiently distant from each other in the solution to be considered as separated reactants. A schematic representation for the ONIOM Bulk reaction with its transition state is represented in Figure 7b.

By employing this procedure, we determined that the Bulk reaction possesses an energy barrier of 3.33 $kcal.mol^{-1}$ and a reaction energy of $-50.56\ kcal.mol^{-1}$, as depicted in Figure 8a. To further characterize the reaction, we calculated the unimolecular rate coefficients at 298 K, at the CVT/SCT level of theory where the Bulk reaction exhibited a unimolecular coefficient of $8.35 \times 10^{+9}\ s^{-1}$ (Figure 8b). A summary for the detailed rate coefficients obtained at different levels and temperatures are in Tables S19–S21.

In parallel to the ONIOM scheme, we employed the implicit dielectric continuum model (PCM) as a simplifying approximation to understand the solvent's influence on the reaction. Initially, the PCM results revealed that the barrier and reaction energies were aligned with those obtained from gas phase (Figure S9 and Table S24). Thus, the implicit PCM model alone did not provide a comprehensive understanding of the reaction mechanism in the aqueous phase for the ozone-MA system. To address these limitations, we adopted a hybrid approach termed "Bulk-PCM." This approach combines the utilization of a high-level QM within the ONIOM framework, which considers the MA molecule and five explicit water molecules, with the incorporation of the PCM solvation model to describe the surrounding solvent environment (i.e., replacing the low-level QM' region by a PCM) (Figure 7c). In this Bulk-PCM approach, we considered two scenarios: in the first one, denoted as Bulk-PCM_{bi}, a bimolecular reaction was considered with ozone treated within PCM as the first reactant, and MA and five water molecules considered within PCM as the second reactant. However, for the second scenario, denoted as Bulk-PCM_{uni}, we focused on the RC as the initial step, similar to our approach in the unimolecular LH framework.

Figure 6a depicts the relative energy profile for the bimolecular reactions (Bulk-PCM_{bi}): the energy barrier is 2.02 $kcal.mol^{-1}$, along with a reaction energy of $-58.67\ kcal.mol^{-1}$. Compared to the previous surface and gas phase cases, it is evident that the bulk phase favors the reaction, due to the lower energy barrier. Additionally, the bimolecular rate coefficients were calculated under the same conditions (Figure 6b). At 298 K, the Bulk-PCM_{bi} reaction rate coefficient is $5.01 \times 10^{-16}\ cm^3.molecule^{-1}.\ s^{-1}$, which is much faster

than both the surface and gas phase rate coefficients. Furthermore, the computed standard Gibbs free energy (ΔG°) at 298 K between the reactants and the RC was determined to be 6.00 kcal.mol^{-1}, which is lower than the corresponding value observed for surface and gas phases. This finding suggests a more favorable thermodynamic environment in the bulk phase, as emphasized by the K_{eq} and K_c also presented in Table 1.

Next, we examine the second scenario, Bulk-PCM$_{uni}$, which involves a unimolecular reaction and allows for a comparison with the previous LH and Bulk reactions. In Figure 8a, the energy barrier for Bulk-PCM$_{uni}$ is shown to be 4.35 kcal.mol^{-1}, with a reaction energy of −56.35 kcal.mol^{-1}. Notably, both bulk reactions (Bulk and Bulk-PCM$_{uni}$) exhibit lower barriers compared to the LH framework reaction. This difference could be rationalized by monitoring the intramolecular O–H bond that appears to be broken in the bulk compared to gas phase and surface (see Table S27) already for solvated MA. Indeed, the diacid loses the pseudo-conjugate character that was observed for the isolated molecule.

To further characterize the Bulk-PCM$_{uni}$ reaction, Figure 8b presents the rate coefficients obtained using the CVT/SCT method, a comprehensive summary of the results obtained from various methods being shown in Tables S22–S26. It is worth mentioning that all the calculations adhere to the modified Arrhenius equation, as presented in Table 2.

At 298 K, the Bulk-PCM$_{uni}$ rate coefficient is $7.53 \times 10^{+7}$ s^{-1}, i.e., falling between the LH and bulk values. This is consistent with a more favored reaction in the bulk compared to the surface within an aerosol droplet. Then, the corresponding bimolecular rate coefficient (k) can be obtained using Equation (5), leading to a rate coefficient of 1.21×10^{-16} cm^3.molecule^{-1}. s^{-1}. This further emphasizes the relatively faster kinetics of the Bulk-PCM$_{uni}$ reaction when compared to the LH reaction (7.21×10^{-19} cm^3.molecule^{-1}. s^{-1}).

However, it is well known that reactions in aqueous phase may be limited by diffusion processes, leading to an apparent rate coefficient different from the reactive process one. As detailed in the SI (Table S3), the diffusion rate k_D derived from the mutual diffusion coefficients of reactants O_3 and MA is of the order of 6 to 7.5×10^{-12} cm^3.molecule^{-1}. s^{-1} which is much larger than the reaction rate coefficient. This implies that despite ozone's low diffusion toward the bulk phase, as stated by its Henry constant (Anglada et al. 2014; Li, Pak, and Tse 2018; Vácha et al. 2004; Vieceli et al. 2005), once ozone is present in the bulk phase, the Henry constant no longer acts as a key factor restricting the aqueous phase reaction. Consequently, the reaction proceeds without any limitations imposed by diffusion.

Table 3. Reported bimolecular reaction rate coefficients (L.mol^{-1}. s^{-1} and cm^3.molecule^{-1}. s^{-1}) of ozone with maleic acid in aqueous solution compared to present work.

		L.mol^{-1}. s^{-1}	cm^3.molecule^{-1}. s^{-1}
Gas phase		3.9	6.45×10^{-21}
Surface	ER	3.8×10	6.32×10^{-20}
	LH	4×10^2	7.20×10^{-19}
Bulk	Bulk-PCM$_{uni}$	7.3×10^4	1.21×10^{-16}
	Bulk-PCM$_{bi}$	3.02×10^5	5.01×10^{-16}
	Exp.[a]	7.8	1.3×10^{-20}
	Exp.[b]	10^3	1.7×10^{-18}
	Exp.[c]	$(2.4 \pm 0.02) \times 10^4$	$(3.99 \pm 0.03) \times 10^{-17}$
	Exp.[d]	1.2×10^4	2.0×10^{-17}
	Exp.[e]	1.4×10^3	2.3×10^{-18}

[a]($T = 20\,^{\circ}$C, in CCl_4) (Razumovskii and Zaikov 1980); [b](Dianion, pH = 2) (Hoigné and Bader 1983); [c](Dianion) (Pryor, Giamalva, and Church 1984); [d]($T = 20\,^{\circ}$C, pH = 7) (Benbelkacem et al. 2003); [e](Leitzke and Sonntag 2009).

The present calculated bimolecular rate coefficient of 1.21×10^{-16} (Bulk-PCM$_{uni}$) and 7.21×10^{-19} (LH) cm^3.molecule^{-1}. s^{-1} can be compared to previous studies on the ozonolysis of unsaturated maleic acid in aqueous solution (see Table 3). Leitzke and Sonntag reported a reaction rate coefficient of 2.3×10^{-18} cm^3.molecule^{-1}. s^{-1} at pH = 7 (Leitzke and Sonntag 2009). On the other hand, Benbelkacem et al. measured a value of 2.0×10^{-17} cm^3.molecule^{-1}. s^{-1} (Benbelkacem et al. 2003) under conditions of 20 °C and neutral pH. Notably, these two rate coefficients closely approximate the conditions of the present calculations. As our study focuses on comparing reactions in different environments, specifically the surface and bulk phases, we can observe that these reported rate coefficients fall within the range of our surface and bulk values. The other listed rates refer to either a dianion MA system or reactions in CCl_4 and are not directly comparable to the present simulations.

3.3. Atmospheric implication

In summary, Table 3 provides an overview of the bimolecular rate coefficients obtained in this study under various conditions and levels of theory at room temperature. In particular, in the bulk phase, two approaches were investigated: Bulk-PCM$_{bi}$ and Bulk-PCM$_{uni}$. The values obtained for these approaches are 5.01×10^{-16} and 1.21×10^{-16} cm^3.molecule^{-1}. s^{-1}, respectively. Based on these findings, it can be inferred that the ozonolysis of maleic acid primarily occurs preferentially in the bulk phase, where the rate coefficients are faster compared to the surface. This finding is consistent with previous work from Willis

and Wilson (2022) who reported that around 96% of the reactions occur in the bulk droplet, with ozone being depleted to approximately 11% of its concentration deduced from Henry's Law. In addition, even though we can expect an enriched concentration of adsorbed ozone at the interface due to its known surface vs bulk partitioning (Vácha et al. 2004), the surface reaction appears to be slower than in the bulk, with a lower surface affinity of MA compared to bulk. Thus, the reaction rate coefficient is not the only determining factor, partitioning being also a key aspect to account for, but present study clearly shows the importance of treating reactions within a multiphasic framework.

The present results can tentatively be connected to a more global scale through the estimation of atmospheric lifetimes (τ) for multiphase reactions involves analyzing rate coefficients in different environments at various ozone concentration levels. To begin, we employed the bimolecular calculated rate coefficients at 298 K for various tropospheric ozone concentrations and determined the corresponding lifetimes (Figure S10). However, we can focus on the typical ozone concentration of 50 ppb, as indicated by Goldberg et al. (2015). It is evident that the gas phase reaction triggers off the longest lifetimes, which can be attributed to relatively low reaction rates compared to other environments. Regarding the aerosol phase reaction, lifetimes follow the same trend as the rates, where $\tau_{ER} > \tau_{LH}$. Next, for the bulk reaction, we considered the aqueous phase concentration of ozone at the gas-aqueous equilibrium (0.74 ppb) (Chen et al. 2008). The lifetime of the bulk reaction ranges from 31 to 127 h for Bulk-PCM_{bi} and Bulk-PCM_{uni}, respectively. These rather long lifetimes in the bulk can be attributed to the lower concentration of O_3 in the aqueous phase.

The strength of the present multilevel theoretical approach relies on the explicit description of the environment, i.e., aqueous phase, and the possibility to distinguish surface and bulk reactions. Besides, the combination of an appropriate DFT functional with single point high level *ab initio* provides a precise determination of the energetics along the reaction path and consequently of the rate coefficients, which are obtained using sophisticated methods as well. Even though calculations have been performed for the three distinct scenarios, namely gas phase, surface and bulk, only one initial geometry, obtained *via* classical molecular dynamics, has been investigated. The statistics could certainly be improved by exploring various initial geometries extracted along the MD trajectory and computing the full reaction path. This configuration exploration would however be computationally demanding. For example, the number of configurations needed to obtain a target accuracy on energy barriers has been discussed by Ryde in a biomolecules context (Ryde 2017): even for a typical chemical accuracy of 1 kcal/mol (which approximately translate into 1 order of magnitude variation of the rate coefficient), a rather huge number of sample geometries is required. This could be achieved by reducing the cost of the quantum chemical methods (e.g., using semi-empirical or DFTB), but at the risk of getting inaccurate results, especially for pre-reactive complexes and in case of low barriers.

Interestingly, the proposed methodology could nevertheless be extended to other systems where in particular morphology of the particulate phase, solid or viscous could influence significantly the reactivity by slowing diffusion (Kaur Kohli et al. 2023) or constraining the geometries to less favorable ones, therefore leading to slower rates. In that spirit, Marshall et al. (2018) pointed out the influence of particle viscosity on the ozonolysis of maleic acid in ternary aerosol particles containing water and sucrose. Furthermore, the effect of a coating at the aerosol surface could also be investigated by this multimethod approach since it has been shown that the ozone trapping ability of aerosol surfaces is influenced by the simultaneous presence of both water and organic acids (see, e.g., Li et al. 2019). This study paves the way for further investigations into heterogeneous reactivities, considering various factors (multiphase processes, surface propensity, diffusion, mixing and coating effects, pH).

4. Conclusion

In this study, we have examined at the molecular scale the physicochemical properties and kinetics of heterogeneous ozone oxidation of aerosol particles containing maleic acid, utilizing both classical and quantum approaches. Our investigation encompassed not only the reactions occurring within the bulk of droplets but also those transpiring at the droplet surface treating these environments with specific arrangements of molecules. Aqueous phase ozonolysis of maleic acid in the atmosphere can be categorized into distinct scenarios. These include interfacial reactions, such as Eley–Rideal (ER), less probable, and Langmuir–Hinshelwood (LH) mechanisms, as well as the bulk aqueous phase reaction. The surface reaction rate coefficient depends on several parameters which are not straightforward to determine accurately such as

the reaction rate coefficient, the appropriate thickness for the surface layer as well as the surface concentration of reactants. Moreover, a critical aspect influencing the collision rate between ozone and a maleic acid molecule is the availability of the π double bonds at the surface. The results obtained from the present description of maleic acid at the surface of an aerosol phase demonstrated the enhancing effect of water molecules on the reactions between ozone and maleic acid. These water molecules facilitated the formation of the primary-ozonide (POZ) at the surface of the aerosol droplet.

This work also shows that the heterogeneous reaction of ozone with maleic acid aerosol particles is dominated by bulk phase reactions, as indicated by the high rate coefficients observed in the bulk, which is determined to be in the order of 1.21×10^{-16} cm^3.molecule^{-1}. s^{-1}, indicating extremely high ozonolysis rate coefficients in this environment. As a consequence, the amount of ozone participating in bulk aqueous phase reactions becomes the main bottleneck for these reactions. The determined surface (7.20×10^{-19} cm^3.molecule^{-1}. s^{-1}) and bulk reaction rate coefficients (5.01×10^{-16} and 1.21×10^{-16} cm^3.molecule^{-1}. s^{-1}) fall into the range of previously measured experimental rates obtained for similar conditions (neutral pH, …).

However, while we provided a molecular-scale study of the primary-ozonide formation in the reaction of ozone with maleic acid, further investigations are needed to understand the subsequent steps after primary ozonolysis, including the fate of Criegee intermediates (Khan et al. 2018) and the formation of final products, especially for surface and bulk cases. Indeed, building on the findings of Gallimore et al. (2011), it is evident that aqueous phase ozonolysis of maleic acid produces condensed phase products, such as oxalic and glyoxylic acids. Consequently, further research is needed to determine whether the products remain in the condensed phase or transfer to the surface, and whether there are further reactions between these reaction products and gas phase oxidants. Future studies could also explore similar systems, such as fumaric acid, which lack the intramolecular bond present in maleic acid and have been already studied experimentally (Nájera, Percival, and Horn 2009, 2010). This comparison could offer valuable insights into how the presence or absence of this bond affects reaction rate coefficients and mechanisms. These efforts will contribute to advancing our understanding the behavior of aerosols in the environment and their impact on atmospheric processes.

Disclosure statement

No potential conflict of interest was reported by the author(s).

Funding

The authors received the financial support from the CaPPA project (Chemical and Physical Properties of the Atmosphere) funded by the French National Research Agency (ANR) through the PIA (Programme d'Investissement d'Avenir) under Contract No. ANR-10-LABX-005; the Région Hauts de France and the Ministère de l'Enseignement Supérieur et de la Recherche (CPER ECRIN) and the European Fund for Regional Economic Development. This work was performed using HPC resources from GENCI-TGCC (Grant No. 2022-A0110801859) and the Center de Ressources Informatiques (CRI) of the Université de Lille.

ORCID

Rawan AbouHaidar http://orcid.org/0009-0004-6449-1889
Denis Duflot http://orcid.org/0000-0002-8307-5344
Céline Toubin http://orcid.org/0000-0002-7379-8178

References

Adler, T. B., G. Knizia, and H.-J. Werner. 2007. A simple and efficient CCSD(T)-F12 approximation. *J. Chem. Phys.* 127 (22):221106. doi: 10.1063/1.2817618.

Alang, A. K., S. G. Aggarwal, K. Singh, D. Soni, and K. Kawamura. 2023. Water-soluble dicarboxylic acids, oxoacids and α-dicarbonyls in the tropical aerosols in coastal megacity Mumbai: Molecular characteristics and formation processes. *J. Atmos. Chem.* 80 (2):137–55. doi: 10.1007/s10874-022-09442-3.

Anglada, J. M., M. Martins-Costa, M. F. Ruiz-López, and J. S. Francisco. 2014. Spectroscopic signatures of ozone at the air-water interface and photochemistry implications. *Proc. Natl. Acad. Sci. U S A* 111 (32):11618–23. doi: 10.1073/pnas.1411727111.

Bao, J. L., and D. G. Truhlar. 2017. Variational transition state theory: Theoretical framework and recent developments. *Chem. Soc. Rev.* 46 (24):7548–96. doi: 10.1039/C7CS00602K.

Bayly, C. I., P. Cieplak, W. Cornell, and P. A. Kollman. 1993. A well-behaved electrostatic potential based method using charge restraints for deriving atomic charges: The RESP model. *J. Phys. Chem.* 97 (40):10269–80. doi: 10.1021/j100142a004.

Benbelkacem, H., H. Cano, S. Mathe, and H. Debellefontaine. 2003. Maleic acid ozonation: Reactor modeling and rate coefficients determination. *Ozone Sci. Eng.* 25 (1):13–24. doi: 10.1080/713610647.

Berendsen, H. J. C., J. R. Grigera, and T. P. Straatsma. 1987. The missing term in effective pair potentials. *J. Phys. Chem.* 91 (24):6269–71. doi: 10.1021/j100308a038.

Berendsen, H. J. C., J. P. M. Postma, W. F. van Gunsteren, A. DiNola, and J. R. Haak. 1984. Molecular dynamics with coupling to an external bath. *J. Chem. Phys.* 81 (8): 3684–90. doi: 10.1063/1.448118.

Berthelot, D. 1889. Sur le Mélange des Gaz. *C. R. Acad. Sci. Paris* 126:1703.

Beste, A., and A. C. I. Buchanan. 2010. Substituent effects on the reaction rates of hydrogen abstraction in the pyrolysis of phenethyl phenyl ethers. *Energy Fuels* 24 (5): 2857–67. doi: 10.1021/ef1001953.

Chapleski, R. C., Y. Zhang, D. R. Troya, and J. Morris. 2016. Heterogeneous chemistry and reaction dynamics of the atmospheric oxidants, O 3, NO 3, and OH, on organic surfaces. *Chem. Soc. Rev.* 45 (13):3731–46. doi: 10.1039/C5CS00375J.

Chan, L. P., and C. K. Chan. 2012. Roles of the phase state and water content in ozonolysis of internal mixtures of maleic acid and ammonium sulfate particles. *Aerosol Sci. Technol.* 46 (7):781–93. doi: 10.1080/02786826.2012.665514.

Chen, Z. M., H. L. Wang, L. H. Zhu, C. X. Wang, C. Y. Jie, and W. Hua. 2008. Aqueous-phase ozonolysis of methacrolein and methyl vinyl ketone: A potentially important source of atmospheric aqueous oxidants. *Atmos. Chem. Phys.* 8 (8):2255–65. doi: 10.5194/acp-8-2255-2008.

Chung, L. W., W. Sameera, M. C. Ramozzi, R. Page, A. J. Hatanaka, M. Petrova, G. P. Harris, T. V. Li, X. Ke, Z. Liu, et al. 2015. The ONIOM method and its applications. *Chem. Rev.* 115 (12):5678–796. doi: 10.1021/cr5004419.

Cieplak, P., W. D. Cornell, C. Bayly, and P. A. Kollman. 1995. Application of the multimolecule and multiconformational RESP methodology to biopolymers: Charge derivation for DNA, RNA, and proteins. *J. Comput. Chem.* 16 (11):1357–77. doi: 10.1002/jcc.540161106.

Cossi, M., N. Rega, G. Scalmani, and V. Barone. 2003. Energies, structures, and electronic properties of molecules in solution with the C-PCM solvation model. *J. Comput. Chem.* 24 (6):669–81. doi: 10.1002/jcc.10189.

Criegee, R. 1975. Mechanism of ozonolysis. *Angew. Chem. Int. Ed. Engl.* 14 (11):745–52. doi: 10.1002/anie.197507451.

Dash, M. R., M. Balaganesh, and B. Rajakumar. 2014. Rate coefficients for the gas-phase reaction of OH radical with α-pinene: An experimental and computational study. *Mol. Phys.* 112 (11):1495–511. doi: 10.1080/00268976.2013.840395.

Dash, M. R., and S. S. Mishra. 2022. Mechanistic and kinetic approach on methyl isocyanate (CH3NCO) with OH and Cl. *Mol. Phys.* 120 (21):e2124933. doi: 10.1080/00268976.2022.2124933.

Davidson, E. R., and D. Feller. 1986. Basis set selection for molecular calculations. *Chem. Rev.* 86 (4):681–96. doi: 10.1021/cr00074a002.

Dennis-Smither, B. J., F. H. Marshall, R. E. H. Miles, T. C. Preston, and J. P. Reid. 2014. Volatility and oxidative aging of aqueous maleic acid aerosol droplets and the dependence on relative humidity. *J. Phys. Chem. A* 118 (30):5680–91. doi: 10.1021/jp504823j.

dos Santos, A. P., M. Girotto, and Y. Levin. 2016. Simulations of Coulomb systems with slab geometry using an efficient 3D Ewald summation method. *J. Chem. Phys.* 144 (14):144103. doi: 10.1063/1.4945560.

Einstein, A. 1905. Über die von der molekularkinetischen Theorie der Wärme geforderte Bewegung von in ruhenden Flüssigkeiten suspendierten Teilchen. *Ann. Phys.* 322 (8):549–60. doi: 10.1002/andp.19053220806.

Frisch, M. J., G. W. Trucks, H. B. Schlegel, G. E. Scuseria, M. A. Robb, J. R. Cheeseman, G. Scalmani, V. Barone, G. A. Petersson, H. Nakatsuji, et al. 2016. *Gaussian 16 Rev. C.01*.

Fukui, K. 1981. The path of chemical reactions - the IRC approach. *Acc. Chem. Res.* 14 (12):363–8. doi: 10.1021/ar00072a001.

Gallimore, P. J., P. Achakulwisut, F. D. Pope, J. F. Davies, D. R. Spring, and M. Kalberer. 2011. Importance of relative humidity in the oxidative ageing of organic aerosols: Case study of the ozonolysis of maleic acid aerosol. *Atmos. Chem. Phys.* 11 (23):12181–95. doi: 10.5194/acp-11-12181-2011.

Goldberg, D. L., T. P. Vinciguerra, K. M. Hosley, C. P. Loughner, T. P. Canty, R. J. Salawitch, and R. R. Dickerson. 2015. Evidence for an increase in the ozone photochemical lifetime in the eastern United States using a regional air quality model. *JGR. Atmos.* 120 (24):12778–93. doi: 10.1002/2015JD023930.

Grira, A., C. Amarandei, C. Roman, O. Bejaoui, N. Aloui, G. El Dib, C. Arsene, I. G. Bejan, R. I. Olariu, A. Canosa, et al. 2022. Gas-phase ozone reaction kinetics of C5–C8 unsaturated alcohols of biogenic interest. *J. Phys. Chem. A* 126 (27):4413–23. doi: 10.1021/acs.jpca.2c02805.

Hess, B., Bekker, H. Berendsen, H. J. C, and Fraaije, J. G. E. M. 1997. LINCS: A linear constraint solver for molecular simulations. *J. Comput. Chem.* 18 (12):1463–72. doi: 10.1002/(SICI)1096-987X(199709)18:12<1463::AID-JCC4>3.0.CO;2-H.

Hoigné, J., and H. Bader. 1983. Rate coefficients of reactions of ozone with organic and inorganic compounds in water—I: Non-dissociating organic compounds. *Water Res.* 17 (2):173–83. doi: 10.1016/0043-1354(83)90098-2.

Huang, J.-H., F. Zhang, Y.-P. Shi, J.-R. Cai, Y.-H. Chuang, W.-P. Hu, Y.-Y. Lee, and C. C. Wang. 2023. Water plays multifunctional roles in the intervening formation of secondary organic aerosols in ozonolysis of limonene: A valence photoelectron spectroscopy and density functional theory study. *J. Phys. Chem. Lett.* 14 (15):3765–76. doi: 10.1021/acs.jpclett.3c00560.

IPCC (Intergovernmental Panel on Climate Change), ed. 2023. Technical summary. In *Climate change 2021 – The physical science basis: Working group I contribution to the sixth assessment report of the intergovernmental panel on climate change*, 35–144. Cambridge, UK: Cambridge University Press.

Irrgang, M. E., J. M. Hays, and P. M. Kasson. 2018. gmxapi: A high-level interface for advanced control and extension of molecular dynamics simulations. *Bioinformatics* 34 (22):3945–7. doi: 10.1093/bioinformatics/bty484.

Jorgensen, W. L., J. P. Ulmschneider, and J. Tirado-Rives. 2004. Free energies of hydration from a generalized born model and an all-atom force field. *J. Phys. Chem. B* 108 (41):16264–70. doi: 10.1021/jp0484579.

Kanakidou, M., J. H. Seinfeld, S. N. Pandis, I. Barnes, F. J. Dentener, M. C. Facchini, R. Van Dingenen, B. Ervens, A. Nenes, C. J. Nielsen, et al. 2005. Organic aerosol and global climate modelling: A review. *Atmos. Chem. Phys.* 5 (4):1053–123. doi: 10.5194/acp-5-1053-2005.

Kannath, S., P. Adamczyk, D. Ferro-Costas, A. Fernández-Ramos, D. T. Major, and A. Dybala-Defratyka. 2020. Role of microsolvation and quantum effects in the accurate prediction of kinetic isotope effects: The case of hydrogen atom abstraction in ethanol by atomic hydrogen in aqueous solution. *J. Chem. Theory Comput.* 16 (2): 847–59. doi: 10.1021/acs.jctc.9b00774.

Kaur Kohli, R., R. S. Reynolds, K. R. Wilson, and J. F. Davies. 2023. Exploring the influence of particle phase in the ozonolysis of oleic and elaidic acid. *Aerosol Sci. Technol.* 0 (0):1–18. doi: 10.1080/02786826.2023.2226183.

Khan, M. a H., C. J. Percival, R. L. Caravan, C. A. Taatjes, and D. E. Shallcross. 2018. Criegee intermediates and their impacts on the troposphere. *Environ. Sci. Process. Impacts.* 20 (3):437–53. doi: 10.1039/C7EM00585G.

Klamt, A., C. Moya, and J. Palomar. 2015. A comprehensive comparison of the IEFPCM and SS(V)PE continuum solvation methods with the COSMO approach. *J. Chem. Theory Comput.* 11 (9):4220–5. doi: 10.1021/acs.jctc.5b00601.

Kleber, J., K. Laß, and G. Friedrichs. 2013. Quantitative time-resolved vibrational sum frequency generation spectroscopy as a tool for thin film kinetic studies: New insights into oleic acid monolayer oxidation. *J. Phys. Chem. A* 117 (33):7863–75. Accessed June 12, 2023. https://pubs.acs.org/doi/pdf/10.1021/jp404087s. doi: 10.1021/jp404087s.

Knizia, G., and H.-J. Werner. 2008. Explicitly correlated RMP2 for high-spin open-shell reference states. *J. Chem. Phys.* 128 (15):154103. doi: 10.1063/1.2889388.

Kroll, J. H., and J. H. Seinfeld. 2008. Chemistry of secondary organic aerosol: Formation and evolution of low-volatility organics in the atmosphere. *Atmos. Environ.* 42 (16):3593–624. doi: 10.1016/j.atmosenv.2008.01.003.

Leitzke, A., and C. V. Sonntag. 2009. Ozonolysis of unsaturated acids in aqueous solution: acrylic, methacrylic, maleic, fumaric and muconic acids. *Ozone Sci. Eng.* 31 (4):301–8. doi: 10.1080/01919510903041354.

Li, W., C. Y. Pak, and Y.-L. S. Tse. 2018. Free energy study of H2O, N2O5, SO2, and O3 gas sorption by water droplets/slabs. *J. Chem. Phys.* 148 (16):164706. doi: 10.1063/1.5022389.

Li, W., C. Y. Pak, X. Wang, and Y.-L. S. Tse. 2019. Uptake of common atmospheric gases by organic-coated water droplets. *J. Phys. Chem. C* 123 (31):18924–31. doi: 10.1021/acs.jpcc.9b03252.

Lily, M., B. Baidya, W. Wang, F. Liu, and A. K. Chandra. 2020. Atmospheric chemistry of CHF2CF2OCH2CF3: Reactions with Cl atoms, fate of CHF2CF2OC•HCF3 radical, formation of OH radical and Criegee intermediate. *Atmos. Environ.* 242:117805. doi: 10.1016/j.atmosenv.2020.117805.

Lorentz, H. A. 1881. Ueber die Anwendung des Satzes vom Virial in der kinetischen Theorie der Gase. *Ann. Phys.* 248 (1):127–36. doi: 10.1002/andp.18812480110.

Ma, Q., M. Schwilk, C. Köppl, and H.-J. Werner. 2017. Scalable electron correlation methods. 4. Parallel explicitly correlated local coupled cluster with pair natural orbitals (PNO-LCCSD-F12). *J. Chem. Theory Comput.* 13 (10): 4871–96. doi: 10.1021/acs.jctc.7b00799.

Maçôas, E. M. S., R. Fausto, J. Lundell, M. Pettersson, L. Khriachtchev, and M. Räsänen. 2001. A matrix isolation spectroscopic and quantum chemical study of fumaric and maleic acid. *J. Phys. Chem. A* 105 (15):3922–33. doi: 10.1021/jp003802p.

Marshall, F. H., T. Berkemeier, M. Shiraiwa, L. Nandy, P. B. Ohm, C. S. Dutcher, and J. P. Reid. 2018. Influence of particle viscosity on mass transfer and heterogeneous ozonolysis kinetics in aqueous–sucrose–maleic acid aerosol. *Phys. Chem. Chem. Phys.* 20 (22):15560–73. doi: 10.1039/C8CP01666F.

Miertuš, S., E. Scrocco, and J. Tomasi. 1981. Electrostatic interaction of a solute with a continuum. A direct utilization of AB initio molecular potentials for the prevision of solvent effects. *Chem. Phys.* 55 (1):117–29. doi: 10.1016/0301-0104(81)85090-2.

Nájera, J. J., C. J. Percival, and A. B. Horn. 2009. Infrared spectroscopic studies of the heterogeneous reaction of ozone with dry maleic and fumaric acid aerosol particles. *Phys. Chem. Chem. Phys.* 11 (40):9093–103. doi: 10.1039/B909623J.

Nájera, J. J., C. J. Percival, and A. B. Horn. 2010. Kinetic studies of the heterogeneous oxidation of maleic and fumaric acid aerosols by ozone under conditions of high relative humidity. *Phys. Chem. Chem. Phys.* 12 (37): 11417–27. doi: 10.1039/B924775K.

Nikitin, T., S. Lopes, and R. Fausto. 2022. Matrix isolation study of fumaric and maleic acids in solid nitrogen. *J. Phys. Chem. A* 126 (27):4392–412. doi: 10.1021/acs.jpca.2c02770.

Pavarelli, G., J. Velasquez Ochoa, A. Caldarelli, F. Puzzo, F. Cavani, and J.-L. Dubois. 2015. A new process for maleic anhydride synthesis from a renewable building block: The gas-phase oxidehydration of bio-1-butanol. *ChemSusChem* 8 (13):2250–9. doi: 10.1002/cssc.201500095.

Peterson, K. A., T. B. Adler, and H.-J. Werner. 2008. Systematically convergent basis sets for explicitly correlated wavefunctions: The atoms H, He, B–Ne, and Al–Ar. *J. Chem. Phys.* 128 (8):084102. doi: 10.1063/1.2831537.

Pfeifle, M., Y.-T. Ma, A. W. Jasper, L. B. Harding, W. L. Hase, and S. J. Klippenstein. 2018. Nascent energy distribution of the Criegee intermediate CH2OO from direct dynamics calculations of primary ozonide dissociation. *J. Chem. Phys.* 148 (17):174306. doi: 10.1063/1.5028117.

Pope, F. D., P. J. Gallimore, S. J. Fuller, R. A. Cox, and M. Kalberer. 2010. Ozonolysis of maleic acid aerosols: Effect upon aerosol hygroscopicity, phase and mass. *Environ. Sci. Technol.* 44 (17):6656–60. doi: 10.1021/es1008278.

Pöschl, U. 2005. Atmospheric aerosols: Composition, transformation, climate and health effects. *Angew. Chem. Int. Ed. Engl.* 44 (46):7520–40. doi: 10.1002/anie.200501122.

Pryor, W. A., D. H. Giamalva, and D. F. Church. 1984. Kinetics of ozonation. 2. Amino acids and model compounds in water and comparisons to rates in nonpolar solvents. *J. Am. Chem. Soc.* 106 (23):7094–100. doi: 10.1021/ja00335a038.

Pye, H. O. T., A. Nenes, B. Alexander, A. P. Ault, M. C. Barth, S. L. Clegg, J. L. Collett, Jr., K. M. Fahey, C. J. Hennigan, H. Herrmann, et al. 2020. The acidity of atmospheric particles and clouds. *Atmos. Chem. Phys.* 20 (8):4809–88. doi: 10.5194/acp-20-4809-2020.

Razumovskii, S. D., and G. E. Zaikov. 1980. Kinetics and mechanism of the reaction of ozone with double bonds.

Russ. Chem. Rev. 49 (12):1163–80. doi: 10.1070/RC1980v049n12ABEH002535.

Riipinen, I., T. Yli-Juuti, J. R. Pierce, T. Petäjä, D. R. Worsnop, M. Kulmala, and N. M. Donahue. 2012. The contribution of organics to atmospheric nanoparticle growth. *Nature Geosci.* 5 (7):453–8. doi: 10.1038/ngeo1499.

Rosenfeld, D., S. Sherwood, R. Wood, and L. Donner. 2014. Climate effects of aerosol-cloud interactions. *Science* 343 (6169):379–80. doi: 10.1126/science.1247490.

Ryde, U. 2017. How many conformations need to be sampled to obtain converged QM/MM energies? The curse of exponential averaging. *J. Chem. Theory Comput.* 13 (11):5745–52. doi: 10.1021/acs.jctc.7b00826.

Salta, Z., M. Vega-Teijido, A. Katz, N. Tasinato, V. Barone, and O. N. Ventura. 2022. Dipolar 1,3-cycloaddition of thioformaldehyde S-methylide (CH2 SCH2) to ethylene and acetylene. A comparison with (valence) isoelectronic O3, SO2, CH2 OO and CH2 SO. *J. Comput. Chem.* 43 (21):1420–33. doi: 10.1002/jcc.26946.

Sato, K., F. Ikemori, S. Ramasamy, A. Fushimi, K. Kumagai, A. Iijima, and Y. Morino. 2021. Four- and five-carbon dicarboxylic acids present in secondary organic aerosol produced from anthropogenic and biogenic volatile organic compounds. *Atmosphere* 12 (12):1703. doi: 10.3390/atmos12121703.

Schank, K. 2004. Der Mechanismus der Alken-Ozonolyse – eine kritische Betrachtung. *Helv. Chim. Acta* 87 (8):2074–84. doi: 10.1002/hlca.200490186.

Schwilk, M., Q. Ma, C. Köppl, and H.-J. Werner. 2017. Scalable electron correlation methods. 3. Efficient and accurate parallel local coupled cluster with pair natural orbitals (PNO-LCCSD). *J. Chem. Theory Comput.* 13 (8):3650–75. doi: 10.1021/acs.jctc.7b00554.

Sempere, R., and K. Kawamura. 1996. Low molecular weight dicarboxylic acids and related polar compounds in the remote marine rain samples collected from Western Pacific. *Atmos. Environ.* 30 (10-11):1609–19. doi: 10.1016/1352-2310(95)00436-X.

Shiraiwa, M., K. Ueda, A. Pozzer, G. Lammel, C. J. Kampf, A. Fushimi, S. Enami, A. M. Arangio, J. Fröhlich-Nowoisky, Y. Fujitani, et al. 2017. Aerosol health effects from molecular to global scales. *Environ. Sci. Technol.* 51 (23):13545–67. doi: 10.1021/acs.est.7b04417.

Srivastava, D., T. V. Vu, S. Tong, Z. Shi, and R. M. Harrison. 2022. Formation of secondary organic aerosols from anthropogenic precursors in laboratory studies. *Npj Clim. Atmos. Sci.* 5 (1):1–30. doi: 10.1038/s41612-022-00238-6.

Stewart, A. C., M. J. Paterson, and S. J. Greaves. 2022. The influence of saturation on the surface structure of mixed fatty acid-on-water aerosol: A molecular dynamics study. *Environ. Sci: Atmos.* 2 (6):1516–25. doi: 10.1039/D2EA00089J.

Stokes, G. G. 1901. *Mathematical and physical papers*. Vol. 3, 38–54. Cambridge University Press.

Tomasi, J., B. Mennucci, and R. Cammi. 2005. Quantum mechanical continuum solvation models. *Chem. Rev.* 105 (8):2999–3093. doi: 10.1021/cr9904009.

Truhlar, D. G., and B. C. Garrett. 1984. Variational transition state theory. *Annu. Rev. Phys. Chem.* 35 (1):159–89. doi: 10.1146/annurev.pc.35.100184.001111.

Truhlar, D. G., B. C. Garrett, and S. J. Klippenstein. 1996. Current status of transition-state theory. *J. Phys. Chem.* 100 (31):12771–800. doi: 10.1021/jp953748q.

Truhlar, G., and B. C. Garrett. 1987. Dynamical bottlenecks and semiclassical tunneling paths for chemical reactions. *J. Chim. Phys.* 84:365–9. doi: 10.1051/jcp/1987840365.

Truong, T. N. 1994. A direct ab initio dynamics approach for calculating thermal rate coefficients using variational transition state theory and multidimensional semiclassical tunneling methods. An application to the CH4 + H↔CH3 + H2 reaction. *J. Chem. Phys.* 100 (11):8014–25. doi: 10.1063/1.466795.

Vácha, R., P. Slavíček, M. Mucha, B. J. Finlayson-Pitts, and P. Jungwirth. 2004. Adsorption of atmospherically relevant gases at the air/water interface: Free energy profiles of aqueous solvation of N2, O2, O3, OH, H2O, HO2, and H2O2. *J. Phys. Chem. A* 108 (52):11573–9. doi: 10.1021/jp046268k.

Vieceli, J., M. Roeselová, N. Potter, L. X. Dang, B. C. Garrett, and D. J. Tobias. 2005. Molecular dynamics simulations of atmospheric oxidants at the air – water interface: Solvation and accommodation of OH and O3. *J. Phys. Chem. B* 109 (33):15876–92. doi: 10.1021/jp051361+.

Wang, G., and K. Kawamura. 2005. Molecular characteristics of urban organic aerosols from Nanjing: A case study of a mega-city in China. *Environ. Sci. Technol.* 39 (19):7430–8. doi: 10.1021/es051055+.

Wang, X., J. Sun, D. Han, L. Bao, Q. Mei, B. Wei, Z. An, M. He, S. Yuan, J. Xie, et al. 2020. Gaseous and heterogeneous reactions of low-molecular-weight (LMW) unsaturated ketones with O3: Mechanisms, kinetics, and effects of mineral dust in tropospheric chemical processes. *Chem. Eng. J.* 395:125083. doi: 10.1016/j.cej.2020.125083.

Wang, X., Y. Wei, H. Zhang, L. Bao, M. He, and S. Yuan. 2021. Understanding the properties of methyl vinyl ketone and methacrolein at the air-water interface: Adsorption, heterogeneous reaction and environmental impact analysis. *Chemosphere* 283:131183. doi: 10.1016/j.chemosphere.2021.131183.

Werner, H.-J., P. J. Knowles, F. R. Manby, J. A. Black, K. Doll, A. Heßelmann, D. Kats, A. Köhn, T. Korona, D. A. Kreplin, et al. 2020. The Molpro quantum chemistry package. *J. Chem. Phys.* 152 (14):144107. doi: 10.1063/5.0005081.

Wheeler, S. E., D. H. Ess, and K. N. Houk. 2008. Thinking out of the black box: Accurate barrier heights of 1,3-dipolar cycloadditions of ozone with acetylene and ethylene. *J. Phys. Chem. A* 112 (8):1798–807. doi: 10.1021/jp710104d.

Willis, M., and K. Wilson. 2022. Coupled interfacial and bulk kinetics govern the timescales of multiphase ozonolysis reactions. *J. Phys. Chem. A* 126 (30):4991–5010. doi: 10.26434/chemrxiv-2022-k2snf.

Wojcieszak, R., F. Santarelli, S. Paul, F. Dumeignil, F. Cavani, and R. V. Gonçalves. 2015. Recent developments in maleic acid synthesis from bio-based chemicals. *Sustain. Chem. Process.* 3 (1):9. doi: 10.1186/s40508-015-0034-5.

Wright, S., and D. G. Leaist. 1998. Diffusion of weak acids in salt solutions maleic acid + NaCl + water. *Faraday Trans.* 94 (10):1457–63. doi: 10.1039/a800424b.

Yeh, I.-C., and M. L. Berkowitz. 1999. Ewald summation for systems with slab geometry. *J. Chem. Phys.* 111 (7):3155–62. doi: 10.1063/1.479595.

Zhang, J., Jim, Wei, Y, and Fang, Z. 2019. Ozone pollution: A major health hazard worldwide. *Front. Immunol.* 10: 2518. () doi: 10.3389/fimmu.2019.02518.

Zhao, Y., and D. G. Truhlar. 2008a. Density functionals with broad applicability in chemistry. *Acc. Chem. Res.* 41 (2):157–67. doi: 10.1021/ar700111a.

Zhao, Y., and D. G. Truhlar. 2008b. The M06 suite of density functionals for main group thermochemistry, thermochemical kinetics, noncovalent interactions, excited states, and transition elements: Two new functionals and systematic testing of four M06-class functionals and 12 other functionals. *Theor. Chem. Account.* 120 (1-3):215–41. doi: 10.1007/s00214-007-0310-x.

Zheng, J., J. L. Bao, R. Meana-Pañeda, S. Zhang, B. J. Lynch, J. C. Corchado, Y.-Y. Chuang, P. L. Fast, W.-P. Hu, Y.-P. Liu, et al. 2017. *Polyrate-version 2017-C.* Minneapolis, MN: University of Minnesota.

Zheng, J., and D. G. Truhlar. 2010. Kinetics of hydrogen-transfer isomerizations of butoxyl radicals. *Phys. Chem. Chem. Phys*. 12 (28):7782–93. doi: 10.1039/B927504E.